Carcinogenesis, 2020, Vol. 41, No. 7, 865–874

doi:10.1093/carcin/bgz191
Advance Access Publication November 18, 2019
Original Article

ORIGINAL ARTICLE

Regulation of cell–cell adhesion in prostate cancer cells by microRNA-96 through upregulation of E-Cadherin and EpCAM

Gjendine Voss[1], Benedikta S.Haflidadóttir[1], Helena Järemo[2], Margareta Persson[1], Tina Catela Ivkovic[1,3], Pernilla Wikström[2] and Yvonne Ceder[1,*]

[1]Department of Laboratory Medicine, Lund University, Lund, Sweden, [2]Department of Medical Biosciences, Umeå University, Umeå, Sweden and [3]Division of Molecular Medicine, Ruder Boskovic Institute, Zagreb, Croatia

*To whom correspondence should be addressed. Tel: +46 46 2226452; Email: yvonne.ceder@med.lu.se

Abstract

Prostate cancer is one of the most common cancers in men, yet the biology behind lethal disease progression and bone metastasis is poorly understood. In this study, we found elevated levels of microRNA-96 (miR-96) in prostate cancer bone metastasis samples. To determine the molecular mechanisms by which miR-96 deregulation contributes to metastatic progression, we performed an Argonaute2-immunoprecipitation assay, in which mRNAs associated with cell–cell interaction were enriched. The expression of two cell adhesion molecules, E-Cadherin and EpCAM, was upregulated by miR-96, and potential targets sites were identified in the coding sequences of their mRNAs. We further showed that miR-96 enhanced cell–cell adhesion between prostate cancer cells as well as their ability to bind to osteoblasts. Our findings suggest that increased levels of miR-96 give prostate cancer cells an advantage at forming metastases in the bone microenvironment due to increased cell–cell interaction. We propose that miR-96 promotes bone metastasis in prostate cancer patients by facilitating the outgrowth of macroscopic tumours in the bone.

Introduction

Prostate cancer is the most common cancer affecting men in Europe, killing over 100 000 European men every year (1). While localised prostate cancer is often slow-growing and clinically manageable, chances of survival are diminished upon metastatic dissemination, and treatment is rarely curative (2).

During the process of metastasis, the cells have to leave the primary tumour and enter the blood stream or nearby lymph vessels by breaking cell–cell contacts, degrading the surrounding matrix and migrating through the tissue. After travelling through the circulatory system, the cells must be able to leave the vessels and invade the potential secondary sites. There, they have to evade the local immune system, and ultimately proliferate and form a tumour mass in order to colonise the metastatic niche (3). These complex processes demand vastly different abilities from a tumour cell. Successful metastasis is therefore the result of a chain of dramatic remodelling events of the cancer cell's biology.

One class of molecules that can facilitate and regulate such complex biological changes is that of microRNAs (miRNAs), constituting short non-coding RNAs that can regulate many different targets at once. In the cytoplasm, miRNAs are incorporated into Argonaute (Ago) protein complexes which bind transcripts and inhibit or enhance their expression, either through modulation of mRNA stability or translation rate (4).

Several miRNAs have been shown to be involved in cancer development and are being explored for cancer therapy (5–7). One of these miRNAs is microRNA-96 (miR-96), which we and others have shown to promote proliferation through repression of the tumour suppressor FOXO1 in prostate cancer and other cancers, for example, breast and liver (8–10). This has inspired efforts to develop therapeutics that target miR-96 (11). In prostate cancer, miR-96 has also been shown to downregulate the expression of other tumour suppressors, such as ETV6 and MTSS1, activate

Received: April 17 2019; **Revised:** October 24 2019; **Accepted:** November 15 2019

Abbreviations

Ago	Argonaute
CDS	coding sequence
miRNA	microRNA
TSBs	target site blockers;
UTR	untranslated region

the mTOR pathway through inhibiting AKT1S1, and regulate autophagy and androgen signalling (12–16). Measurable deregulation of miR-96 in tumour tissue has been reported by us and several other groups in cancer, indicating that miR-96 also has potential as a diagnostic and prognostic biomarker (9,17).

Here, we show that miR-96 is enriched in prostate cancer bone metastases compared to primary tumours. We further find E-Cadherin and EpCAM to be upregulated, potentially by binding of miR-96 to target sites in the coding sequences, leading to increased cell–cell adhesion. Taken together, we propose that miR-96 plays a role in secondary tumour formation at bone metastatic sites.

Materials and methods

Patient samples

Cohort 1 consists of 49 samples from transurethral resections of the prostate that were collected in Malmö 1990–99, with complete follow-up. The cohort is extensively described in Hagman *et al.* (18). However, for analysis regarding treatment 42 patients were used, and when analysing metastatic status 45 patients were analysed (due to missing data for seven and four patients, respectively). Cohort 2 consists of 55 freshly frozen bone metastasis samples (three of which were hormone-naïve, two had recently started androgen deprivation and 50 were castration-resistant) that were obtained from prostate cancer patients during surgery for spinal cord compression, as previously described (19,20). Cohort 2 also included prostate tumour samples from 12 separate patients treated with radical prostatectomy as well as 13 samples of adjacent non-cancerous prostate tissue (19).

Cohort 3 is an external cohort published by Taylor *et al.* (21). Data for miRNA and mRNA expression profiles were extracted from NCBI GEO (GSE21032) for 111 prostate cancer samples (98 primary tumours, 13 metastases) and 28 matching non-cancerous prostate samples.

Ethics statement

All studies using patient material adhered to the Helsinki declaration and were approved by the local ethics committees, Regionala etikprövningsnämnden i Lund for Cohort 1 (LU445-07) and Regionala etikprövningsnämnden i Umeå for Cohort 2 (03-185).

RNA extraction, reverse transcription and qRT-PCR of patient samples

In Cohort 1, small RNAs were extracted from prostate tissue FFPE sections using a modified protocol of the mirVana miRNA Isolation kit (Ambion®, Austin, TX) as described previously (18). Quantification of miRNAs was performed on 5 ng small RNAs using TaqMan MicroRNA assays (Applied Biosystems, Foster City, CA) on a 7900 HT Real-Time PCR System (Applied Biosystems), as described by Larne *et al.* (17).

In Cohort 2, small RNAs were isolated from bone metastasis and primary tumour samples by RNA extraction using the AllPrep protocol (Qiagen, Stockholm, Sweden), as described by Ylitalo *et al.* (20), and enriched and purified using the RNeasy MinElute Cleanup kit (Qiagen) according to the manufacturer's description. Quantification of miRNAs in 12.5 ng total RNA was performed using TaqMan MicroRNA assays (Applied Biosystems) on a QuantStudio 7 Flex machine (Applied Biosystems) according to the manufacturer's instructions. Samples were run in quadruplicates and calculations were based on the comparative ΔCt method.

For both cohorts, miR-96 (#000186) levels were normalised to the geometric mean of U47 (#001223), RNU48 (#001006) and RNU66 (#001002).

Cell culture and transfection

Prostate cancer cell lines DU145, 22Rv1 and PC3 were obtained from the American Type Culture Collection, and the cells were cultured according to the supplier's recommendations. The cell lines were authenticated by STR profiling (most recently in 2017–18) and regularly tested for mycoplasma contamination (most recently in 2019) throughout the study. Human primary mesenchymal stem cells were a kind gift from Dr. Stefan Scheding (Lund University).

The mesenchymal stem cells were expanded using StemMACS expansion medium (Miltenyi, Bergisch-Gladbach, Germany) and differentiated into osteoblasts in low glucose DMEM with 10% FBS with addition of 10 mM β-glycerophosphate, 0.05 mM L-ascorbic acid and 0.1 μM dexamethasone (all Sigma–Aldrich, Steinheim, Germany). The differentiation was verified after 3 weeks by staining with 10 mg/ml Alizarin Red S (Sigma–Aldrich). Osteoblast-conditioned medium was collected after at least 48 h and cleared by centrifugation at 900×*g*. For experiments in conditioned medium, 50% conditioned and 50% fresh medium were used, with 50% prostate cancer cell-conditioned medium in the control wells.

Cells were transiently transfected with miRIDIAN microRNA mimics for hsa-miR-96-5p (C-300514-07, Dharmacon, Lafayette, CO) or miRIDIAN microRNA Mimic Negative Control #1 (CN-001000-01, Dharmacon) at 120 nM. For miR-96 inhibition, miRCURY LNA Inhibitors for hsa-miR-96-5p (410467-00, Exiqon) and miRCURY LNA Inhibitor Negative Control A (199004-00, Exiqon) were used at 120 nM, unless otherwise stated. Transfection was performed using Oligofectamine reagents (Invitrogen, Carlsbad, CA). Assays were performed 72 h (for DU145) or 96 h (for 22Rv1) after transfection unless otherwise specified.

Potential target sites for miR-96 in *CDH1* and *EPCAM* mRNA were predicted using the DIANA microT-CDS algorithm and RNA22 (22–24). Target site blockers (TSBs) for *CDH1* mRNA were Custom LNA Oligonucleotides (Exiqon, Vedbaek, Denmark) designed to block the predicted target site in the *CDH1* coding sequence (CDS). A Custom LNA Oligonucleotide designed to block the predicted miR-650 target site in *KLK3* mRNA was used as a negative control. TSBs for *EPCAM* mRNA were miRCURY LNA Power TSBs (Exiqon), designed to bind the two predicted target sites in the *EPCAM* CDS, with miRCURY LNA Power TSB Negative Control A (Exiqon) as a negative control. Target sites, TSBs and LNA spike-in patterns are shown in Supplementary Figure 1. For co-transfection with TSBs, 100 nM miRNA mimics were used and TSBs were added at 100 nM (*EPCAM* mRNA) or 300 nM (*CDH1* mRNA).

Immunoprecipitation of human AGO2 complexes

The immunoprecipitation protocol was adapted from previously described procedures (25,26). Cells were trypsinised 48 h after transfection with miR-96 mimic or negative control, and washed with cold PBS before lysis of the cells (20 mM Tris–HCl pH 7.5, 150 mM NaCl, 0.3% Nonidet P-40, 2 mM EDTA, 1 mM NaF, 1 mM DTT, Halt™ Protease Inhibitor Cocktail (Thermo Scientific, Rockford, IL), 50 U/ml SUPERase In RNase Inhibitor [Ambion®, Life Technologies, NY]). The lysate was kept on ice for 30 min before centrifugation at 10 000×*g* for 30 min at 4°C. To reduce background signal, the lysate was pre-cleared with beads blocked with 1 mg/ml yeast tRNA (Applied Biosystems) and 1 mg/ml RNase-free BSA for 30 min on rotation at 4°C, before incubation with antibody against human AGO2 (11A9, IgG2a, Ascenion, Germany) on rotation overnight at 4°C (27). The next day, the mixture was incubated with Protein G Sepharose 4 fast flow beads (GE Healthcare, Fairfield, CT) on rotation at 4°C for 2 h. The samples were washed four times with wash buffer (50 mM Tris–HCl pH 7.5, 500 mM NaCl, 0.3% Nonidet P-40, 1 mM $MgCl_2$, 50 U/ml SUPERase In) and once with PBS. The protein/RNA complexes were digested with 40 μg Proteinase K (Qiagen, Hilden, Germany) in 30 mM Tris–HCl pH 8.0, 10 mM EDTA, 1% SDS buffer for 30 min at 50°C. RNA was isolated by phenol–chloroform extraction and EtOH precipitation as described earlier (28). The RNA concentration was measured using a NanoDrop spectrophotometer (ND-1000, Thermo Scientific, Wilmington, DE) and RNA quality was assessed using an Agilent 2100 Bioanalyzer (Agilent, Santa Clara, CA).

Microarray hybridisation and data analysis

Microarray hybridisation and analysis were performed at SCIBLU Genomics, Lund. Single-stranded cDNA was generated using the

GeneChip® Whole Transcript cDNA Synthesis and Amplification Kit (Affymetrix, Santa Clara, CA) using 100 ng of total RNA. Amplified cDNA was fragmented and labelled using the GeneChip® Whole Transcript Terminal Labelling Kit (Affymetrix). Subsequently, the biotinylated cDNA was hybridised to GeneChip® Human Gene 1.0 ST-v1 Arrays (Affymetrix) according to the manufacturer's recommendations. Arrays were scanned using the GeneChip® Scanner 3000 and image analysis was performed using GeneChip® Operating Software (Affymetrix) and Genepix® 4.0 (Axon Instruments).

The Basic Affymetrix Chip and Experimental Quality Analyses were performed, and the data were normalised and summarised using the Robust Multichip Average algorithm in Expression Console Software v1.1.2 (Affymetrix). The data were analysed using SAM analysis to identify significantly differentially expressed genes between the groups using TMEV v4.0 software. All genes enriched upon miR-96 transfection with $q < 5$ were analysed through Ingenuity Pathway Analysis (Ingenuity® Systems, Qiagen, Redwood City, CA). A score reflecting the negative logarithm of the P-value was subsequently computed for each network according to the fit of the original set of significantly different genes.

RNA extraction, reverse transcription and qRT-PCR of cells

Total RNA of cells transiently transfected with miR-96 or negative control mimics was extracted using TRIzol reagent (Ambion, Carlsbad, CA) according to the manufacturer's recommendations. For measuring mRNA baseline expression in six prostate cancer cell lines, we used a panel of previously isolated total RNA (8). RNA concentrations were measured using NanoDrop.

The samples were treated with DNase I (Thermo Scientific, Vilnius, Lithuania) and cDNA was synthesised using the RevertAid H Minus First Strand cDNA Synthesis kit (Thermo Scientific) with 0.5 µl Oligo(dT) and 0.5 µl Random Hexamer primers according to the manufacturer's instructions.

Gene expression was quantified using TaqMan™ Gene Expression Master Mix and TaqMan™ gene expression assays (all Applied Biosystems). *CDH1* (Hs01023894_m1) and *EPCAM* (Hs00158980_m1) mRNA levels were normalised to the geometric mean of *GUSB* (Hs99999908_m1) and *PGK1* (Hs99999906_m1) mRNA levels. qRT-PCR was performed on QuantStudio 7 Flex.

For determination of miR-96 levels in cells, reverse transcription of 100 ng total RNA was performed using the TaqMan MicroRNA Reverse Transcription Kit (Applied Biosystems) according to the manufacturer's instructions. Quantification of miR-96, U47, RNU48 and RNU66 was performed using TaqMan assays and protocols as described above for patient samples.

Western blot

Cells were transiently transfected with miR-96 mimic or negative control, and protein lysates were harvested using M-PER Mammalian Protein Extraction Reagent supplemented with Halt™ Protease Inhibitor cocktail (1:100) and 5 mM EDTA (all Thermo Scientific). Cell debris was removed by centrifugation at 14 000×*g* at 4°C for 10 min. Protein concentrations were determined using Coomassie Plus Bradford Assay Reagent (Thermo Scientific).

Equal amounts of protein were supplemented with 4× Laemmli Loading buffer (Bio-Rad, Hercules, CA) containing DTT and incubated at 95°C for 5 min. Protein samples were electrophoretically separated on 4–20% Mini-PROTEAN® TGX™ precast gels (Bio-Rad) and transferred to PVDF membranes using the TransBlot® Turbo™ Transfer System (Bio-Rad). PageRuler Prestained Protein Ladder (Thermo Scientific) was used as a molecular weight marker. The membranes were blocked with 5% milk and probed with primary antibodies overnight at 4°C. Primary antibodies were anti-CDH1 (sc-8426, Santa Cruz Biotechnology, Dallas, TX; 1:500), anti-EPCAM (sc-25308, Santa Cruz Biotechnology; 1:500), anti-GAPDH (MAB374, Merck Millipore, Darmstadt, Germany; 1:10 000), and anti-α-Actinin (sc-17829, Santa Cruz Biotechnology; 1:500). Polyclonal Goat Anti-Mouse Immunoglobulins/HRP (P0447, DAKO, Glostrup, Denmark) was used as a secondary antibody, diluted 1:5000. Chemiluminescence from HRP-coupled secondary antibodies was recorded using Luminata Forte Western HRP substrate (Millipore, Billerica, MA) and an Amersham Imager 600 (GE Healthcare, Chicago, IL). Semi-quantification of western blots was performed using ImageJ (29). For figures, contrast and brightness of the whole images was adjusted to improve clarity and the blots were cropped. The whole blots are shown, together with the molecular weight marker, in Supplementary Figures 4–6.

Luciferase assay

The 3′untranslated region (UTR) sequence of the *CDH1* gene (nucleotides 2799–4780 of *CDH1* mRNA, NM_004360.4) and nucleotides 1856–2574 of the CDS (nucleotides 1982–2700 of *CDH1* mRNA; containing the predicted miR-96 binding site) were cloned into the pMIR-REPORT luciferase vector. Co-transfection of the pMIR-REPORT firefly luciferase vector, a pRL vector encoding Renilla luciferase (a kind gift from Prof Lars Rönnstrand, Lund University), and miR-96 or negative control mimics was performed. For the luciferase vector containing the CDS, cells were co-transfected with TSBs. The cells were harvested 24 h after transfection and firefly luciferase and Renilla luciferase signals were measured on a Wallac 1420 Victor2 reader (Perkin Elmer) using the Dual-Luciferase® Reporter Assay System (Promega, Madison, WI).

Flow cytometry

Cells were transiently transfected with miR-96 or negative control mimics. After 72 h, the cells were trypsinised, washed with PBS, and stained with anti-EpCAM APC (#347200, BD Biosciences, Franklin Lakes, NJ) in FACS buffer (PBS with 1% FBS, 2 mM EDTA) for 1 h on ice. Control cells were stained with APC Mouse IgG1, κ Isotype Control (#555751, BD Biosciences). After staining, the cells were washed twice with PBS and re-suspended in FACS buffer. Cells were analysed using a BD FACSCanto™ II (BD Biosciences). For estimating the proportion of $EpCAM^{high}$ and $EpCAM^{low}$ cells, the cut-off was chosen so that approximately 50% of cells would be $EpCAM^{high}$ and 50% of cells would be $EpCAM^{low}$ in negative control cells. Data analysis was performed using FlowJo software (FlowJo LLC, Ashland, OR).

Adhesion assays

Cell–cell adhesion was measured by two methods. For both assays, cells were transfected with miR-96 or negative control mimics and detached using Versene (Gibco, Grand Island, NY). For the cell clustering assay, 80 000 cells were incubated in a microcentrifuge tube at 37°C with mild rolling for 4.5 h. Cells were then transferred to a glass slide and numbers of cell clusters and single cells were counted.

In the assay for attachment to monolayers, cells were washed with PBS and stained with BCECF AM (2′,7′-bis(2-carboxyethyl)-5-(and-6)-carboxyfluorescein, Acetoxymethyl Ester; Live Technologies, Eugene, OR) diluted 1:400 in PBS. After incubation at 37°C for 15 min, cells were washed twice and fluorescence was measured to assist with normalisation of cell counts. Equal numbers of cells (40 000 for DU145, 50 000 for 22Rv1) were transferred to confluent monolayers of untransfected DU145 cells in a 24-well cell culture plate and incubated at 37°C for 5 h. The cells were harvested by incubation with 100 µl 1× passive lysis buffer (Promega, Madison, WI) for 15 min at room temperature. From each sample, 45 µl duplicates were measured on a Wallac 1420 Victor2 microplate reader (Perkin Elmer, Waltham, MA; excitation 290 nm, emission 535 nm).

Colony formation assay

Anchorage-independent colony formation in soft agar was assayed in 6-well plates. The base layer was prepared as 0.5% agarose in complete medium. For the top layer, 1000 cells were resuspended in 0.3% agarose in growth medium (either 100% fresh medium, or 50% fresh medium and 50% osteoblast-conditioned medium). Liquid medium was added on top of the agarose layer to prevent drying out and was replenished weekly. After 4 weeks, wells were rinsed with PBS and fixed with cold methanol for 10 min. Colonies were stained with 0.05% crystal violet in 20% methanol for 30 min and rinsed with water. The colonies were counted under a microscope in 10 fields per well.

Statistical analysis

All statistical analysis was performed using GraphPad Prism version 7.00 (GraphPad Software, La Colla, CA). For the patient cohorts, groups of

interest were compared using a Mann–Whitney *U*-test. Linear regression and calculations of Pearson correlation coefficients were used to analyse Cohort 3. All *in vitro* experiments were analysed using two-tailed unpaired Student's *t*-tests, except the luciferase assays, which were evaluated using one-way ANOVAs and pair-wise comparisons for groups of interest using Sidak's multiplicity correction. For all statistical tests, $\alpha = 0.05$ was chosen as the significance level.

Results

miR-96 is upregulated in bone metastasis samples

High miR-96 levels have previously been associated with high WHO grade and shorter overall survival in prostate cancer (8). This prompted us to investigate if miR-96 is involved in castration resistance and metastasis, other hallmarks of aggressive prostate cancer with large clinical impact. We analysed data from Cohort 1 consisting of 49 prostate cancer patients in Malmö, Sweden and found miR-96 levels to be significantly higher in castration-resistant prostate cancer compared to hormone-naïve prostate cancer (Figure 1A; $^{*}P = 0.0172$) (17,18). In the same cohort, miR-96 levels in the primary tumours of patients that developed metastasis were statistically significantly higher compared to patients that did not develop metastasis or in which metastasis was not suspected and therefore not assessed (Figure 1B; $^{*}P = 0.0495$).

Due to the small size of Cohort 1 and as high levels of miR-96 in the primary tumour do not necessarily equal elevated levels or a biological role at the site of metastasis, we investigated miR-96 expression in bone metastasis tissues in Cohort 2 from Umeå, Sweden (19,20). The bone metastasis tissues expressed significantly higher levels of miR-96 than the primary tumours (Figure 1C; $^{*}P = 0.0202$), suggesting that miR-96 can promote formation of bone metastases.

To elucidate the mechanisms through which miR-96 acts in this setting, we performed Ago2-immunoprecipitation on miR-96-transfected DU145 prostate cancer cells, and analysed the mRNAs enriched in miR-96:Ago2 complexes on a microarray. We performed Ingenuity pathway analysis on genes enriched in miR-96-transfected cells compared to the control and found several cancer pathways to be enriched (Table 1), for example, cell cycle, which is consistent with the previously described effect on proliferation through FOXO1 (8–10). Interestingly, the top enriched pathway was cell–cell interaction and movement, and on the list of enriched mRNAs E-Cadherin (*CDH1*) mRNA and Epithelial Cell Adhesion Molecule (*EPCAM*) mRNA were found in the top 25 (Table 2). E-Cadherin and EPCAM play a pivotal role in cell–cell adhesion (30,31), leading us to explore their potential regulation through miR-96.

In Cohort 3 with 111 prostate cancer patients, miR-96 levels were found to be associated with the levels of *CDH1* and *EPCAM* mRNA (Figures 1D and E; $^{***}P = 0.0001$ and $^{***}P < 0.0001$, respectively), strengthening the notion that miR-96 can regulate these targets in a clinical setting (21).

miR-96 targets and upregulates E-Cadherin

We selected two prostate cancer cell lines, DU145 and 22Rv1, in order to investigate the broader biological effect of miR-96 in prostate cancer rather than in one limited cellular context. DU145 cells have low baseline expression of miR-96, E-Cadherin mRNA and EpCAM mRNA, and 22Rv1 cells have high baseline expression of all three RNAs (Figures 2A and 3A). Furthermore, DU145 cells are AR-negative and 22Rv1 cells are AR-positive, so the two cell lines represent different types of prostate cancer.

After transfection with miR-96 mimics (Supplementary Figure 2A), E-Cadherin levels were upregulated at the mRNA and protein level in both cell lines (Figures 2B and C; $^{*}P = 0.0484$ (mRNA) and $^{***}P = 0.0006$ (protein) for DU145; $^{**}P = 0.0055$ (mRNA) and $^{**}P = 0.0084$ (protein) for 22Rv1), with a stronger effect in DU145 cells.

Next, we searched for predicted miR-96 target sites in the *CDH1* mRNA using the Diana MicroT-CDS algorithm. Several target sites were predicted, both in the CDS and in the 3′UTR (Figure 2D). To determine which part of the mRNA E-Cadherin regulation is mediated through, we performed luciferase reporter assays with both the 3′UTR and the CDS cloned into luciferase reporter vectors in PC3 cells co-transfected with miR-96 mimics. We chose these cells because they have very low E-Cadherin baseline expression (Figure 2A), so that any interference by the endogenous transcript would be minimal. There was no difference in relative luciferase expression from the 3′UTR-containing vector upon miR-96 transfection (Figure 2E; $P = 0.5808$). However, there was an increase of relative luciferase expression upon miR-96 transfection in experiments with the CDS-containing vector (Figure 2F; $^{***}P < 0.0001$). This increase was reduced by co-transfection with TSBs designed to block the predicted target site in the CDS (Figure 2D, Supplementary Figure 1A; $^{***}P < 0.0001$), implying action of miR-96 through this binding site. We confirmed this finding with Western blots, where the TSB partially abolished the upregulation of E-Cadherin protein by miR-96 mimics (Figure 2G).

miR-96 targets and upregulates EpCAM

Already when investigating baseline levels of EpCAM expression in our panel of cell lines, we noticed an association between EpCAM levels and miR-96 levels, where cell lines with high miR-96 expression also had higher levels of *EPCAM* mRNA (Figure 3A). When transfecting DU145 and 22Rv1 cells with miR-96 mimics, *EPCAM* mRNA was upregulated, although the effect in 22Rv1 cells was smaller than in DU145 cells (Figure 3B; $^{**}P = 0.0049$ for DU145; $^{**}P = 0.0037$ for 22Rv1). In Western blots, EpCAM protein levels were upregulated in miR-96-transfected DU145 cells (Figure 3C; $^{***}P < 0.0001$), but there was no difference in 22Rv1 cells (Supplementary Figure 2B; $P = 0.5430$). We suggest that due to the high baseline levels of miR-96 and EpCAM expression in these cells, EpCAM production is already saturated.

Interestingly, in experiments with miR-96 inhibitors, we found that inhibiting miR-96 in DU145 cells also increased EpCAM protein expression, but not mRNA expression (Supplementary Figure 2C–E; $^{*}P = 0.0139$ for protein, $P = 0.1736$ for mRNA). In 22Rv1 cells, there was an optimal concentration of miR-96 inhibitors that downregulated EpCAM protein expression, but higher or lower concentrations of inhibitor did not produce an effect (Supplementary Figure 2F). This implies that beyond the mechanism of upregulation of EpCAM mRNA and protein induced by high levels of miR-96 that we are describing here, another mechanism regulating EpCAM protein expression might operate at lower miR-96 levels, which seems highly dependent on miR-96 concentration.

We also performed flow cytometry to confirm that EpCAM upregulation in DU145 cells is reflected on the cell surface (Figure 3D). Upon miR-96 transfection, more cells expressed higher EpCAM levels compared to the control group ($^{***}P = 0.0002$).

We then searched for predicted miR-96 target sites in the *EPCAM* mRNA. While the Diana MicroT-CDS algorithm did not predict any target sites, RNA22 predicted two target sites in the CDS (Figure 3E). We used TSBs to block interaction with these target sites in DU145 cells (Supplementary Figure 1B).

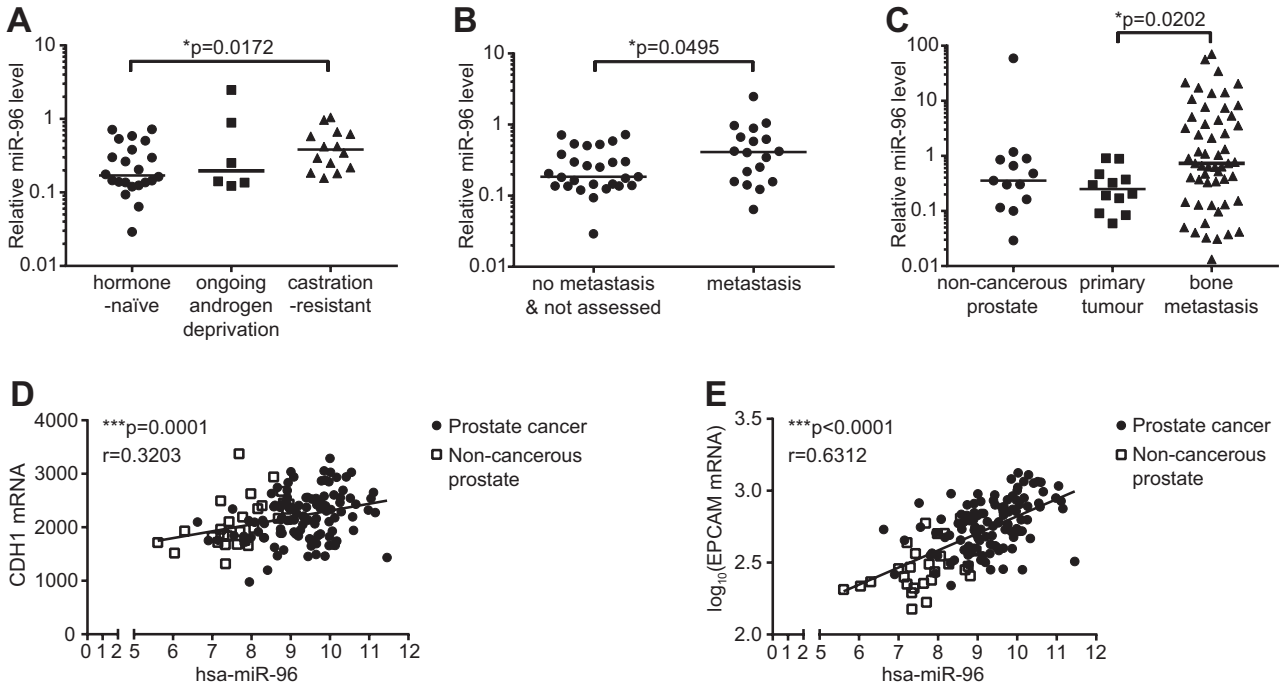

Figure 1. High expression of miR-96 is associated with prostate cancer progression and metastasis. (**A**) Primary tumour miR-96 levels in patients with hormone-naïve or castration-resistant prostate cancer in Cohort 1 ($n = 42$). Shown are median and individual data points for each group and the exact *P* value based on Mann–Whitney *U*-test. (**B**) Primary tumour miR-96 levels in patients without or with metastasis in Cohort 1 ($n = 45$). Shown are median and individual data points for each group and the exact *P* value based on Mann–Whitney *U*-test. (**C**) Levels of miR-96 in bone metastases compared to primary tumours and non-cancerous prostate tissue in Cohort 2 ($n = 80$). Shown are median and individual data points for each group and the exact *P* value of the comparison of interest based on Mann–Whitney *U*-test. (**D**) Association between miR-96 levels and *CDH1* mRNA levels in non-cancerous prostates and prostate cancer in Cohort 3 ($n = 139$). Shown are individual data points and linear regression lines. Correlation coefficients are based on Pearson correlation. (**E**) Association between miR-96 levels and *EPCAM* mRNA levels in non-cancerous prostates and prostate cancer in Cohort 3 ($n = 139$). *EPCAM* mRNA levels were log10-transformed in order to perform meaningful linear regression. Shown are individual data points and linear regression lines. Correlation coefficients are based on Pearson correlation. In all panels, * indicates $P < 0.05$, ** $P < 0.01$, *** $P < 0.001$.

Table 1. Summary of top associated networks in the Ago2-immunoprecipitation assay according to Ingenuity pathway analysis of all mRNAs enriched in miR-96-transfected DU145 cells compared to control cells with $q < 5$

	Associated network functions	Score
1	Cell-to-cell signaling and interaction, tissue development, cellular movement	26
2	DNA replication, recombination and repair, cell cycle, developmental disorder	24
3	Cell cycle, reproductive system disease, cellular function and maintenance	24
4	Cell death, renal necrosis/cell death, cell-mediated immune response	23
5	Gene expression, cancer, cell cycle	23

Co-transfection with TSB1 blocked EpCAM upregulation by miR-96, whereas a 50/50 mixture of both TSBs had a weaker effect and TSB2 alone did not have any effect (Figure 3F). We conclude that the upregulation of EpCAM by miR-96 is mediated through target site 1 in the CDS of *EPCAM* mRNA.

miR-96 enhances cell–cell adhesion

Finally, we investigated if the upregulation of cell adhesion molecules on the surface of miR-96-transfected prostate cancer cells would affect cell adhesion. In a single cell suspension of detached miR-96-transfected DU145 cells incubated for 4.5 h, the miR-96-transfected cells clustered more than the control cells (Figure 4A; $^{**}P = 0.0043$). Confirming this increase in cell–cell adhesion in another assay, we incubated miR-96-transfected cells stained with the fluorescent dye BCECF on prostate cancer cell monolayers and measured how many cells had attached. Relating back to a possible biological role in the establishment of bone metastases, this assay was performed in prostate cancer cell medium as well as in osteoblast-conditioned medium. Cell–cell adhesion was increased in both media and in both DU145 and 22Rv1 cells (Figure 4B; $^{*}P = 0.0101$ (normal medium) and $^{**}P = 0.0035$ (osteoblast-conditioned medium in DU145; $^{*}P = 0.0317$ (normal medium) and $^{**}P = 0.0088$ (osteoblast-conditioned medium) in 22Rv1). In DU145 cells, there was even an overall trend for increased cell–cell adhesion in the osteoblast-conditioned medium, which was then further increased by miR-96 (Figure 4B).

We hypothesised that the increased capacity for cell–cell adhesion of prostate cancer cells with high miR-96 levels allows them to form cell–cell interactions with the surrounding microenvironment and support the cells in forming a new tumour at the site of metastasis. Indeed, miR-96 transfection enhanced DU145 adhesion to monolayers of osteoblasts (Figure 4C; $^{***}P = 0.0003$). Furthermore, although the effect was not

Table 2. Top 25 enriched mRNAs ($q = 0$; sorted by fold change) in Ago2 complexes of miR-96-transfected DU145 cells compared to control cells

	Gene symbol	Gene description	Score (*d*)	Fold change
1	*ADFP*	Adipose differentiation-related protein	7.95	4.48
2	*ACTBL2*	Actin, beta-like 2	7.66	4.33
3	*SELI*	Selenoprotein I	5.20	3.52
4	*DNAJC30*	DnaJ (Hsp40) homolog, subfamily C, member 30	4.58	3.37
5	*DNAJC6*	DnaJ (Hsp40) homolog, subfamily C, member 6	6.05	3.27
6	*CDH1*	Cadherin 1, type 1, E-cadherin (epithelial)	6.26	3.09
7	*HIVEP1*	Human immunodeficiency virus type I enhancer binding protein 1	10.51	3.08
8	*PPM1E*	Protein phosphatase 1E (PP2C domain containing)	5.04	2.91
9	*RC3H2*	Ring finger and CCCH-type zinc finger domains 2	4.28	2.89
10	*HBEGF*	Heparin-binding EGF-like growth factor	5.78	2.89
11	*ALDH9A1*	Aldehyde dehydrogenase 9 family, member A1	4.81	2.62
12	*STAMBPL1*	STAM binding protein-like 1	5.85	2.58
13	*ENC1*	Ectodermal-neural cortex (with BTB-like domain)	6.26	2.55
14	*CRY1*	Cryptochrome 1 (photolyase-like)	4.91	2.55
15	*CCRN4L*	CCR4 carbon catabolite repression 4-like (S. cerevisiae)	4.77	2.38
16	*KLF6*	Kruppel-like factor 6	7.31	2.38
17	*KIAA1147*	KIAA1147	4.52	2.36
18	*GTF2H2*	General transcription factor IIH, polypeptide 2, 44 kDa	4.54	2.34
19	*COL4A3BP*	Collagen, type IV, alpha 3 (Goodpasture antigen) binding protein	6.20	2.27
20	*GTF2H2*	General transcription factor IIH, polypeptide 2, 44 kDa	4.46	2.25
21	*EPCAM*	Epithelial cell adhesion molecule	6.12	2.24
22	*GTF2H2*	General transcription factor IIH, polypeptide 2, 44 kDa	4.37	2.22
23	*PLCB4*	Phospholipase C, beta 4	4.55	2.20
24	*GCNT1*	Glucosaminyl (*N*-acetyl) transferase 1, core 2 (beta-1,6-*N*-acetylglucosaminyltransferase)	4.64	2.19
25	*GTF2H2*	General transcription factor IIH, polypeptide 2, 44 kDa	4.49	2.18

statistically significant in osteoblast-conditioned medium, miR-96-transfected DU145 cells formed more colonies in an anchorage-independent colony formation assay (Figure 4D; $^{**}P = 0.0024$ in normal medium and $P = 0.1641$ in osteoblast-conditioned medium).

Discussion

The role of cell–cell adhesion in cancer metastasis has been much discussed. Traditional models assume that loss of cell–cell adhesion is required to enable extravasation from the primary tumour and subsequent metastasis, and the loss of cell adhesion molecules has been associated with tumour progression (3,30). The transcription factors ZEB1 and SNAIL can induce this epithelial-to-mesenchymal switch (32). Interestingly, ZEB1 has been shown to suppress the expression of miRNAs, including the miR-183-96-182 cluster. In turn, these miRNAs can suppress ZEB1, leading to alleviation of E-Cadherin suppression and thereby E-Cadherin upregulation in breast and colorectal cancer (33,34). This regulation is supported by incidental findings of miR-96 enhancing E-Cadherin expression in bladder cancer cells and CDH1 promoter reporter assays supporting the effect of miR-96 on the transcriptional control of E-Cadherin (35,36). An equivalent mechanism has been described for upregulation of both E-Cadherin and EpCAM expression by miR-200c and miR-205-mediated repression of ZEB1 (37,38), an event that has been associated with prostate cancer development and metastasis (39).

Due to this and other studies, the importance of cell–cell adhesion at the metastatic site is being increasingly recognised. For example, cell–cell contacts are required for proliferation of prostate cancer PDX cells, and especially in bone metastases, the expression of E-Cadherin protein is significantly elevated compared to primary tumours and soft tissue metastases (40,41). In another study, which used different DU145 sublines, only cells with high E-Cadherin expression formed large intratibial lesions. Another subline upregulated E-Cadherin expression up to 10-fold in intratibial tumours, despite sustained ZEB1 expression in these tumours (40). This suggests that ZEB1-mediated mechanisms alone cannot explain the regulation of E-Cadherin expression in prostate cancer.

To our knowledge, E-Cadherin and EpCAM have not been previously described as targets of miR-96 in prostate cancer. Here, we present evidence that miR-96 may directly bind to their mRNAs and increase their expression, which could explain the previously observed ZEB1-independent regulation of E-Cadherin expression in bone metastases (40).

Direct upregulation of targets by miRNAs is rare, but has been associated with cellular stress such as starvation, loss of adhesion, or cell cycle arrest, all of which commonly occur in cancer cells (3,42). This can be mediated through association of Argonaute complexes with proteins other than GW182 such as FXR1 (42), which is in line with miRNA-mediated up rather than downregulation in cellular contexts where GW182 is unavailable (43–45). Interestingly, we found lower mRNA expression of all three GW182 family members in prostate cancer compared to benign prostate samples in Cohort 3 (Supplementary Figure 3), implying that low GW182 levels in prostate cancer cells may be responsible for the positive regulation of E-Cadherin and EpCAM by miR-96. Other described mechanisms for target upregulation by miRNAs are based on inhibition of mechanisms that would otherwise repress mRNA expression, such as the upregulation of 5'TOP mRNAs by miR-10a through alleviation of starvation-induced translational suppression (46), and the prevention of ARE-mediated mRNA decay of IL-10 mRNA through blockage of TTP binding sites by miR-466l (47). In the present study, we have not investigated whether the change in mRNA levels is due to altered mRNA stability, as in this last example, or whether it is due to increased transcriptional activity. If the changed mRNA levels can be attributed to transcriptional changes, this could

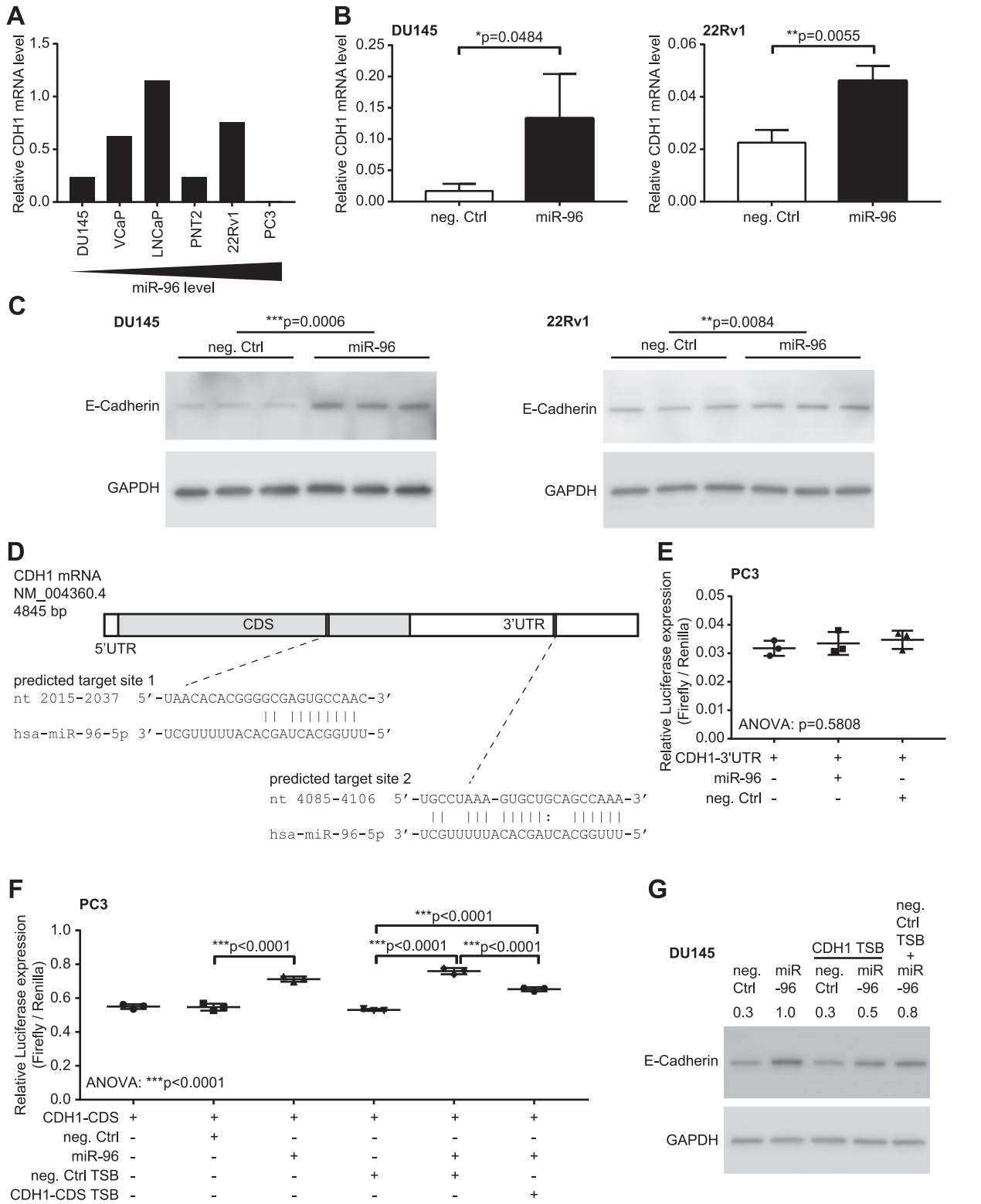

Figure 2. E-Cadherin is upregulated by miR-96. (**A**) *CDH1* mRNA expression in a panel of different cell lines, sorted by increasing miR-96 levels (based on Ref. (8)). (**B**) *CDH1* mRNA expression upon miR-96 transfection in DU145 and 22Rv1 cells. Shown are mean + SD ($n = 3$ per group). Exact *P* values were calculated using two-tailed unpaired student's *t*-test. (**C**) E-Cadherin protein expression upon miR-96 transfection in DU145 and 22Rv1 cells ($n = 3$ per group). Exact *P* values were calculated using two-tailed unpaired student's *t*-test. Uncropped images of the blots including the molecular weight marker are shown in Supplementary Figure 4A and B. (**D**) Predicted miR-96 target sites in *CDH1* mRNA according to the Diana MicroT-CDS algorithm. (**E**) Luciferase reporter assay with the *CDH1* 3′UTR cloned into a firefly luciferase vector. Shown are mean ± SD and individual data points ($n = 3$ per group). Statistical analysis is based on a One-way ANOVA. (**F**) Luciferase reporter assay with the *CDH1* CDS cloned into a firefly luciferase vector. Shown are mean ± SD and individual data points ($n = 3$ per group). Statistical analysis is based on a one-way ANOVA with pair-wise comparisons of interest according to Sidak. (**G**) E-Cadherin protein levels in DU145 cells transfected with miR-96 mimics and *CDH1* CDS TSB. Relative density of normalised protein levels is shown above bands. Uncropped images of the blot including the molecular weight marker are shown in Supplementary Figure 4C. In all panels, * indicates $P < 0.05$, ** $P < 0.01$, *** $P < 0.001$.

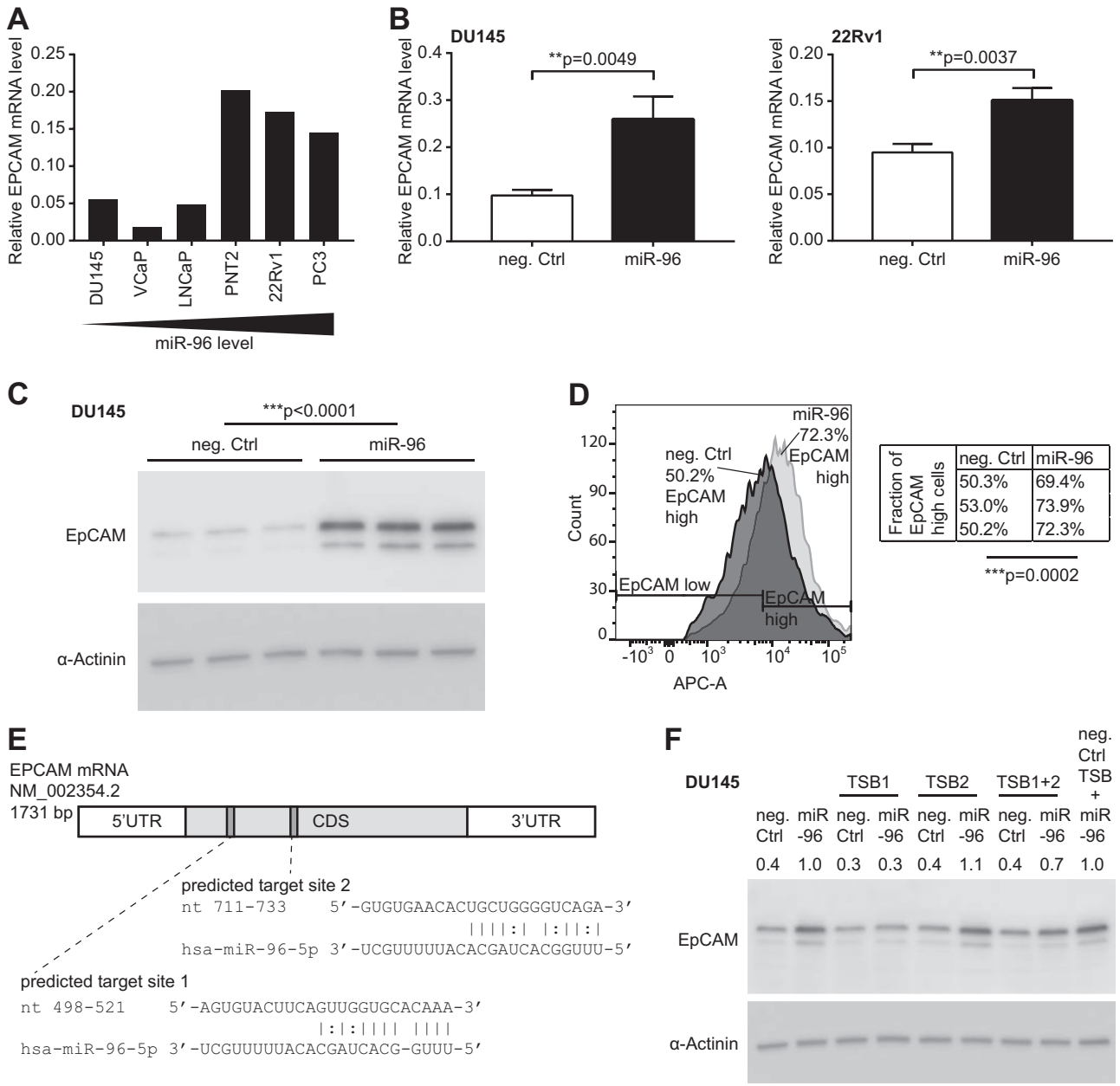

Figure 3. EpCAM is upregulated by miR-96. (**A**) *EPCAM* mRNA expression in a panel of different cell lines, sorted by increasing miR-96 levels (based on Ref. (8)). (**B**) *EPCAM* mRNA expression upon miR-96 transfection in DU145 and 22Rv1 cells. Shown is mean + SD ($n = 3$). Exact *P* values were calculated using two-tailed unpaired Student's *t*-test. (**C**) EpCAM protein levels in miR-96-transfected DU145 cells ($n = 3$ per group). Exact *P* value based on two-tailed unpaired Student's *t*-test. Uncropped images of the blot including the molecular weight marker are shown in Supplementary Figure 5A. (**D**) EpCAM surface expression in miR-96-transfected DU145 cells as measured by flow cytometry. Shown are representative histograms and a summary of the replicates ($n = 3$ per group). Exact *P* value based on two-tailed unpaired Student's *t*-test. (**E**) Predicted miR-96 target sites in *EPCAM* mRNA based on the RNA22 algorithm. (**F**) EpCAM protein levels in DU145 cells transfected with miR-96 mimics and two different EpCAM TSBs. Relative density of normalised protein levels is shown above bands. Uncropped images of the blot including the molecular weight marker are shown in Supplementary Figure 5B. In all panels, * indicates $P < 0.05$, ** $P < 0.01$, *** $P < 0.001$.

point to the indirect mechanism that has been described above. Ultimately, it is likely that multiple mechanisms play a role, both indirect mechanisms such as that mediated by ZEB1, and the target site-mediated effect described by us, the precise mechanism of which would have to be investigated further.

The notion that miR-96 target regulation is mediated through multiple mechanism is supported by the fact that using a TSB to prevent direct interaction with *CDH1* mRNA only partially rescued the effect of miR-96 (Figure 2G), and by the concentration-dependency of the effect of miR-96 on EpCAM regulation (Supplementary Figure 2), implying different mechanisms at different concentrations.

This concentration dependency also cautions against the use of arbitrary concentrations of miRNA mimics and inhibitors without evaluating the effects over a range of concentrations. *In vivo* studies have shown promising results regarding the potential use of miR-96 inhibitors, using either antisense oligonucleotides or small molecule inhibitors targeted to miR-96 (11,15). However, biphasic effects of miR-96 have been reported (15). These concentration-dependent effects may explain why recent

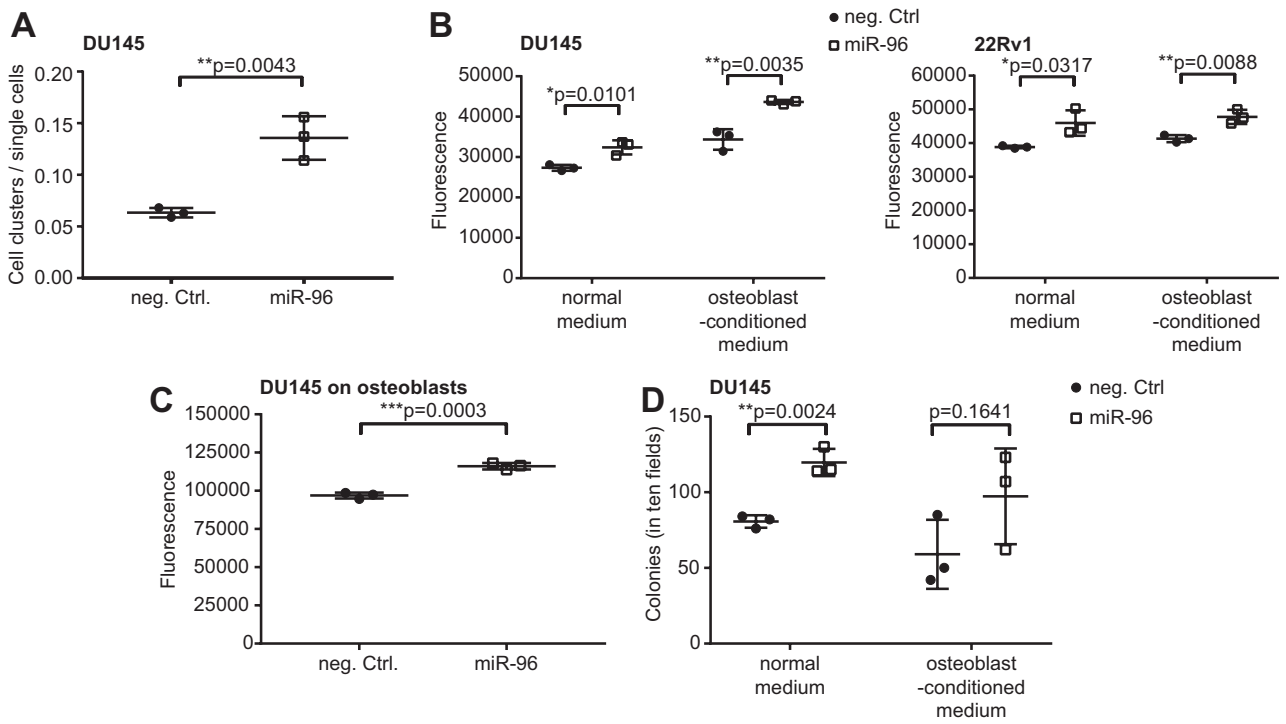

Figure 4. Cell–cell adhesion is enhanced by miR-96. (**A**) Formation of clusters in miR-96 transfected DU145 cells. (**B**) Adhesion of BCECF-labelled miR-96-transfected DU145 and 22Rv1 cells to prostate cancer cell monolayers in normal culture medium and in osteoblast-conditioned medium. (**C**) Adhesion of BCECF-labelled miR-96-transfected DU145 cells to osteoblast monolayers. (**D**) Soft agar colony formation of miR-96-transfected DU145 cells in normal medium and in osteoblast-conditioned medium. All panels show mean ± SD and individual data points ($n = 3$ per group for all experiments). Exact P values are based on two-tailed unpaired Student's t-test. In all panels, * indicates $P < 0.05$, ** $P < 0.01$, *** $P < 0.001$.

efforts to implement miRNA therapies in the clinic have had limited success despite promising results in preclinical models (6,7), as certain therapeutic windows might be missed and side effects might depend on different expression levels in different cell types. Furthermore, if the desired effect only occurs in a narrow concentration range, optimising miRNA delivery approaches and dosage becomes even more relevant.

Lastly, our findings regarding the regulation of EpCAM by miR-96 are also relevant given the use of EpCAM as a marker for circulating tumour cells in the clinical management of prostate cancer, for example, using the FDA-approved CellSearch® technology (48). The miR-96 concentration-dependency and the wide range of EpCAM surface expression levels (Figure 3D) support other publications that warn against the use of EpCAM as a marker for circulating tumour cells due to its heterogeneous expression (49,50).

In this paper, we present evidence that miR-96 can play a role in prostate cancer metastasis. We show that miR-96 levels are higher in bone metastases, and that miR-96 upregulates the two cell adhesion molecules E-Cadherin and EpCAM, rendering cells superior in adhering to osteoblasts and forming colonies in anchorage-deprived conditions. The colonisation of metastatic sites such as the bone is challenging, and we propose that prostate cancer cells with high miR-96 levels have an advantage in forming metastatic tumours due to their increased potential for cell–cell interaction. The implications of our findings for current diagnostic and prognostic standards as well as for the development of miRNA therapies should be explored to ensure optimal patient care.

Supplementary material

Supplementary Figures 1–6 and their legends can be found in Supplementary File 1 at http://carcin.oxfordjournals.org/

Funding

This work was supported by funding from the Swedish Research Council, the European Union Seventh Framework Program (FP7/2007–2013; grant agreement n°201438), Prostatacancerförbundet, BioCARE, and the Swedish Cancer Society.

Acknowledgements

We are very grateful to Prof. Dr. Anders Bjartell for kindly providing us with access to the patient samples in Cohort 1. We also wish to thank Dr. Cecilia Magnusson for providing us with reagents, protocols and technical assistance in the flow cytometry experiment, Dr. Stefan Scheding and Dr. Hongzhe Li for providing us with mesenchymal stem cells, and Prof. Dr. Lars Rönnstrand for giving us the Renilla construct.

Conflict of Interest Statement: None declared.

References

1. Ferlay, J. *et al.* (2018) Cancer incidence and mortality patterns in Europe: estimates for 40 countries and 25 major cancers in 2018. *Eur. J. Cancer*, 103, 356–387.
2. Attard, G. *et al.* (2016) Prostate cancer. *Lancet*, 387, 70–82.
3. Hanahan, D. *et al.* (2011) Hallmarks of cancer: the next generation. *Cell*, 144, 646–674.
4. Pasquinelli, A.E. (2012) MicroRNAs and their targets: recognition, regulation and an emerging reciprocal relationship. *Nat. Rev. Genet.*, 13, 271–282.
5. Catela Ivkovic, T. *et al.* (2017) microRNAs as cancer therapeutics: a step closer to clinical application. *Cancer Lett.*, 407, 113–122.
6. Beg, M.S. *et al.* (2017) Phase I study of MRX34, a liposomal miR-34a mimic, administered twice weekly in patients with advanced solid tumors. *Invest. New Drugs*, 35, 180–188.

7. van Zandwijk, N. *et al*. (2017) Safety and activity of microRNA-loaded minicells in patients with recurrent malignant pleural mesothelioma: a first-in-man, phase 1, open-label, dose-escalation study. *Lancet. Oncol*., 18, 1386–1396.
8. Haflidadóttir, B.S. *et al*. (2013) Upregulation of miR-96 enhances cellular proliferation of prostate cancer cells through FOXO1. *PLoS One*, 8, e72400.
9. Leung, W.K. *et al*. (2015) Wnt/β-Catenin activates MiR-183/96/182 expression in hepatocellular carcinoma that promotes cell invasion. *Cancer Lett*., 362, 97–105.
10. Guttilla, I.K. *et al*. (2009) Coordinate regulation of FOXO1 by miR-27a, miR-96, and miR-182 in breast cancer cells. *J. Biol. Chem*., 284, 23204–23216.
11. Velagapudi, S.P. *et al*. (2016) Design of a small molecule against an oncogenic noncoding RNA. *Proc. Natl. Acad. Sci. U. S. A*., 113, 5898–5903.
12. Tsai, Y.C. *et al*. (2017) Epidermal growth factor receptor signaling promotes metastatic prostate cancer through microRNA-96-mediated downregulation of the tumor suppressor ETV6. *Cancer Lett*., 384, 1–8.
13. Xu, L. *et al*. (2016) miR-96 promotes the growth of prostate carcinoma cells by suppressing MTSS1. *Tumour Biol*., 37, 12023–12032.
14. Siu, M.K. *et al*. (2015) Transforming growth factor-β promotes prostate bone metastasis through induction of microRNA-96 and activation of the mTOR pathway. *Oncogene*, 34, 4767–4776.
15. Ma, Y. *et al*. (2014) Biphasic regulation of autophagy by miR-96 in prostate cancer cells under hypoxia. *Oncotarget*, 5, 9169–9182.
16. Long, M.D. *et al*. (2019) The miR-96 and RARγ signaling axis governs androgen signaling and prostate cancer progression. *Oncogene*, 38, 421–444.
17. Larne, O. *et al*. (2013) miQ—a novel microRNA based diagnostic and prognostic tool for prostate cancer. *Int. J. Cancer*, 132, 2867–2875.
18. Hagman, Z. *et al*. (2010) miR-34c is downregulated in prostate cancer and exerts tumor suppressive functions. *Int. J. Cancer*, 127, 2768–2776.
19. Hörnberg, E. *et al*. (2011) Expression of androgen receptor splice variants in prostate cancer bone metastases is associated with castration-resistance and short survival. *PLoS One*, 6, e19059.
20. Ylitalo, E.B. *et al*. (2017) Subgroups of castration-resistant prostate cancer bone metastases defined through an inverse relationship between androgen receptor activity and immune response. *Eur. Urol*., 71, 776–787.
21. Taylor, B.S. *et al*. (2010) Integrative genomic profiling of human prostate cancer. *Cancer Cell*, 18, 11–22.
22. Miranda, K.C. *et al*. (2006) A pattern-based method for the identification of MicroRNA binding sites and their corresponding heteroduplexes. *Cell*, 126, 1203–1217.
23. Paraskevopoulou, M.D. *et al*. (2013) DIANA-microT web server v5.0: service integration into miRNA functional analysis workflows. *Nucleic Acids Res*., 41(Web Server issue), W169–W173.
24. Reczko, M. *et al*. (2012) Functional microRNA targets in protein coding sequences. *Bioinformatics*, 28, 771–776.
25. Easow, G. *et al*. (2007) Isolation of microRNA targets by miRNP immunopurification. *RNA*, 13, 1198–1204.
26. Peritz, T. *et al*. (2006) Immunoprecipitation of mRNA-protein complexes. *Nat. Protoc*., 1, 577–580.
27. Rüdel, S. *et al*. (2008) A multifunctional human Argonaute2-specific monoclonal antibody. *RNA*, 14, 1244–1253.
28. Chomczynski, P. *et al*. (1987) Single-step method of RNA isolation by acid guanidinium thiocyanate-phenol-chloroform extraction. *Anal. Biochem*., 162, 156–159.
29. Schneider, C.A. *et al*. (2012) NIH Image to ImageJ: 25 years of image analysis. *Nat. Methods*, 9, 671–675.
30. Cavallaro, U. *et al*. (2004) Cell adhesion and signalling by cadherins and Ig-CAMs in cancer. *Nat. Rev. Cancer*, 4, 118–132.
31. Litvinov, S.V. *et al*. (1994) Ep-CAM: a human epithelial antigen is a homophilic cell-cell adhesion molecule. *J. Cell Biol*., 125, 437–446.
32. Peinado, H. *et al*. (2007) Snail, Zeb and bHLH factors in tumour progression: an alliance against the epithelial phenotype? *Nat. Rev. Cancer*, 7, 415–428.
33. Langer, E.M. *et al*. (2018) ZEB1-repressed microRNAs inhibit autocrine signaling that promotes vascular mimicry of breast cancer cells. *Oncogene*, 37, 1005–1019.
34. Li, X.L. *et al*. (2014) A p21-ZEB1 complex inhibits epithelial-mesenchymal transition through the microRNA 183-96-182 cluster. *Mol. Cell. Biol*., 34, 533–550.
35. He, C. *et al*. (2018) miR-96 regulates migration and invasion of bladder cancer through epithelial-mesenchymal transition in response to transforming growth factor-β1. *J. Cell. Biochem*., 119, 7807–7817.
36. Harazono, Y. *et al*. (2013) miR-655 Is an EMT-suppressive microRNA targeting ZEB1 and TGFBR2. *PLoS One*, 8, e62757.
37. Gregory, P.A. *et al*. (2008) The miR-200 family and miR-205 regulate epithelial to mesenchymal transition by targeting ZEB1 and SIP1. *Nat. Cell Biol*., 10, 593–601.
38. Park, S.M. *et al*. (2008) The miR-200 family determines the epithelial phenotype of cancer cells by targeting the E-cadherin repressors ZEB1 and ZEB2. *Genes Dev*., 22, 894–907.
39. Massoner, P. *et al*. (2014) EpCAM is overexpressed in local and metastatic prostate cancer, suppressed by chemotherapy and modulated by MET-associated miRNA-200c/205. *Br. J. Cancer*, 111, 955–964.
40. Putzke, A.P. *et al*. (2011) Metastatic progression of prostate cancer and e-cadherin regulation by zeb1 and SRC family kinases. *Am. J. Pathol*., 179, 400–410.
41. Ruppender, N. *et al*. (2015) Cellular adhesion promotes prostate cancer cells escape from dormancy. *PLoS One*, 10, e0130565.
42. Vasudevan, S. *et al*. (2007) AU-rich-element-mediated upregulation of translation by FXR1 and Argonaute 2. *Cell*, 128, 1105–1118.
43. Yang, Z. *et al*. (2004) GW182 is critical for the stability of GW bodies expressed during the cell cycle and cell proliferation. *J. Cell Sci*., 117(Pt 23), 5567–5578.
44. Mortensen, R.D. *et al*. (2011) Posttranscriptional activation of gene expression in Xenopus laevis oocytes by microRNA-protein complexes (microRNPs). *Proc. Natl. Acad. Sci. U. S. A*., 108, 8281–8286.
45. Zhang, X. *et al*. (2014) MicroRNA directly enhances mitochondrial translation during muscle differentiation. *Cell*, 158, 607–619.
46. Ørom, U.A. *et al*. (2008) MicroRNA-10a binds the 5'UTR of ribosomal protein mRNAs and enhances their translation. *Mol. Cell*, 30, 460–471.
47. Ma, F. *et al*. (2010) MicroRNA-466l upregulates IL-10 expression in TLR-triggered macrophages by antagonizing RNA-binding protein tristetraprolin-mediated IL-10 mRNA degradation. *J. Immunol*., 184, 6053–6059.
48. Galletti, G. *et al*. (2014) Circulating tumor cells in prostate cancer diagnosis and monitoring: an appraisal of clinical potential. *Mol. Diagn. Ther*., 18, 389–402.
49. Grover, P.K. *et al*. (2014) Circulating tumour cells: the evolving concept and the inadequacy of their enrichment by EpCAM-based methodology for basic and clinical cancer research. *Ann. Oncol*., 25, 1506–1516.
50. Gorges, T.M. *et al*. (2012) Circulating tumour cells escape from EpCAM-based detection due to epithelial-to-mesenchymal transition. *BMC Cancer*, 12, 178.